ISSN 1063-7729, Astronomy Reports, 2024, Vol. 68, No. 11, pp. 1076–1090. © Pleiades Publishing, Ltd., 2024.

Measurement of Radio Emission Scattering Parameters in the Direction of Pulsars B0809+74, B0919+06, and B1133+16 with Ground-Space Interferometer RadioAstron

E. N. Fadeev[a,*], A. S. Andrianov[a], M. S. Burgin[a], M. V. Popov[a], A. G. Rudnitskiy[a], T. V. Smirnova[b], and V. A. Soglasnov[a]

[a] *Astro-Space Center, Lebedev Physical Institute, Russian Academy of Sciences, Moscow, Russia*
[b] *Pushchino Radio Astronomical Observatory, Astro-Space Center, Lebedev Physical Institute, Russian Academy of Sciences, Pushchino, Russia*
**e-mail: fadeev@asc.rssi.ru*

Received June 28, 2024; revised August 14, 2024; accepted August 15, 2024

Abstract—We present the analysis of observations of three pulsars at a frequency of 327 MHz with the ground-space interferometer RadioAstron. The main scintillation parameters were measured: the decorrelation bandwidth $\Delta f_{\rm dif}$ and the scintillation time $\Delta t_{\rm dif}$. We have found that these parameters vary significantly over time. For PSR B1133+16, the decorrelation bandwidth $\Delta f_{\rm dif}$ varied from 100 to 350 kHz for the period of 2014 to 2018. For PSR B0919+06 $\Delta f_{\rm dif}$ varied from 36 to 195 kHz over approximately the same time period. In the direction of the observed pulsars, the power-law indices for the spatial inhomogeneity spectrum of the scattering plasma were estimated. The characteristic frequency and time scales of the diffractive scintillations for PSR B0809+74 are comparable to the receiver bandwidth and observation time, respectively. Therefore, only a lower limit for n can be obtained for this pulsar. The mean value is $n = 3.40 \pm 0.11$ for PSR B1133+16 and $n = 3.90 \pm 0.04$ for PSR B0919+06. We have also measured the angular diameter of the average scattering disks, $\theta_{\rm H}$, for these two pulsars. For PSR B0919+06, $\theta_{\rm H}$ = 26–28 mas, and for B1133+16, $\theta_{\rm H} = 12.0 \pm 1.6$ mas. We provide the estimates of the distance to the scattering screens. All measured parameters have been compared with previously published data.

Keywords: interstellar plasma, radio pulsars, interstellar scintillation, VLBI

DOI: 10.1134/S1063772924700951

1. INTRODUCTION

Immediately after the discovery of pulsars, it became clear that these objects could be used to probe the interstellar medium, in particular, to study small-scale turbulence in interstellar plasma, which is impossible to investigate by other means. It turned out that pulsars are ideal point sources, which allow observing the effects of radio wave scattering on fluctuations in electron density down to the smallest scales. In 1967, simultaneously with the discovery of pulsars, the first successful VLBI (Very Long Baseline Interferometry) observations of quasars were conducted, and the idea of a radio interferometer with very long baselines, including intercontinental, and independent recording was realized [1]. Today, VLBI is the primary method for studying the structure of radio sources.

In 2011, the Russian Academy of Sciences and the Federal Space Agency created an orbital space observatory with a 10-m radio telescope, which, in combination with a ground-based network of radio telescopes, formed the ground-to-space interferometer RadioAstron. The space radio telescope orbited the Earth in an elongated elliptical orbit with an apogee distance of 350000 km, which allowed a 25-fold increase in the resolving power of the ground-to-space interferometer compared to a purely ground-based VLBI network. This interferometer operated in four frequency bands: 316–332, 1636–1692, 4804–4860, and 18372–25132 MHz. Over 7 years of operation, many new and unique scientific results were obtained [2, 3].

The 316–332 MHz range was intended for pulsar observations. The priority was the study of radio wave scattering on irregularities in the interstellar plasma along the path from the pulsar to the observer. The observation program included more than 20 bright pulsars. The projections of the ground-to-space interferometer's baseline provided measurements of scattering angles down to fractions of a millisecond of arc.

Table 1. List of observation sessions

Pulsar	Observation date	T_{obs}, min	N_{ch}	P, s	Baseline projection, $D_{\oplus}$	Ground-based telescopes
B0809+74	Dec. 17, 2012	40	4096	1.292241	21.6	GB
	Nov. 24, 2013	120	2048	1.292241	25.2	KL, WB
B0919+06	Apr. 14, 2015	125	2048	0.430627	0.186	AR, GB
	Jan. 11, 2018	120	2048	0.430627	10.3	AR
	May 10, 2018	90	2048	0.430627	11.0	AR, WB
	Nov. 16, 2018	120	2048	0.430627	15.5	AR, SR, WB
	Dec. 15, 2018	120	2048	0.430627	16.1	AR, GB, WB
B1133+16	Feb. 4, 2014	58	8192	1.187913	13.9	KL
	Feb. 3, 2018	120	65536	1.187913	20.6	AR
	Mar. 28, 2018	120	2048	1.187913	21.8	AR
	Dec. 17, 2018	120	2048	1.187913	22.0	AR, GB, WB

T_{obs} is the duration of the observation session, N_{ch} is the number of spectral channels, P is the pulsar period. Baseline projection is the average value of the projection of the ground-space baseline onto the UV plane, expressed in Earth diameters $D_{\oplus}$. For sessions with several ground-based telescopes, the most sensitive telescope was used. In the observation of April 14, 2015 (B0919+06), the projection of the ground baseline is indicated, since there is no interferometric response at both ground-to-space baselines.

As a result of interstellar scattering, the pulsar's image ceases to be a point, and instead, a "scattering disk" with a characteristic angular size, θ_H, appears. A short pulsar pulse acquires an elongated shape with a sharp leading edge followed by an exponential decay with a characteristic duration at the level of $1/e$—the "scattering time," τ_{sc}. The pulsed nature of pulsar emission allows for series of "instantaneous" images of the scattering disk to be obtained, essentially creating a movie rather than a blurred photograph with a long exposure. Through analysis of scattering features with such high angular and temporal resolution, a new effect was discovered—substructure of the scattering disk [4, 5]. The influence of this substructure must be considered when analyzing interferometric data with the highest angular resolution. Anisotropic scattering was detected in the direction of the Vela pulsar [6], and anomalous scattering phenomena were observed in the direction of pulsar B0834+06 [7].

The main method of studying interstellar scattering is through the analysis of "dynamic spectra," which show the evolution of the pulsar's spectral flux density over time. From the analysis of the structure function of the dynamic spectrum, the power-law index of the spatial inhomogeneity spectrum of the scattering plasma can be determined, revealing whether it corresponds to a Kolmogorov, Gaussian, or another type of turbulence spectrum [8].

By analyzing the structure and correlation functions of scattered pulsar radio emission, layers of interstellar plasma near the Solar System that may cause rapid variability of compact extragalactic radio sources were discovered for the first time [9–11]. By comparing the angular sizes of pulsar scattering disks with the characteristic scattering time of pulses, the distances to effective scattering screens were determined. The analysis of these measurements suggests the possible layered structure of interstellar plasma in our Galaxy [4, 12–14].

In this study, we continue the traditional analysis of radio wave scattering features in the direction of pulsars B0809+74, B0919+06, and B1133+16 using the RadioAstron ground-to-space interferometer. The latter two objects have been previously studied by us in several papers [15, 16]. Here, we present new results for B0919+06 and B1133+16. Pulsar B0809+74 has not been studied by us before.

2. OBSERVATIONS AND DATA PROCESSING

The list of observation sessions and their characteristics is provided in Table 1.

In each observation session, in addition to the specified ground-based telescopes, the space telescope (SRT) participated, with its data being transmitted in real time to tracking stations in Pushchino or Green Bank. Ground telescopes that formed the terrestrial arm of the interferometer included the Arecibo telescope (AR), the Robert C. Byrd Green Bank Telescope (GB), the Kalyazin Radio Astronomy Observatory (KL), the Sardinia Radio Telescope (SR), and the Westerbork Synthesis Radio Telescope (WB). After 2015, WB used only one 25-m antenna for interferometry.

Each observation session consisted of individual scans lasting from 10 to 20 min, separated by 30-s technical intervals when no observations were conducted. The typical session duration T_{obs}, ranged from one to two hours, limited by thermal conditions aboard the spacecraft. All sessions were conducted at a center frequency of 324 MHz with a bandwidth $B = 16$ MHz. The number of spectral channels, $N_{\rm ch}$, was chosen during correlation. The signal was recorded in both right and left circular polarizations, except for the observation of pulsar B0809+74 on November 24, 2013, when recording was done in only one polarization. Correlation processing of the data was performed using the ASC correlator, applying incoherent dedispersion and gating mode, where signal correlation occurred only within the pulse window. This window was selected at the 10% level from the peak signal intensity in the average profile. In addition, correlation with identical settings was conducted in two other windows of the same width, positioned at 120° in longitude from the pulse window. The accumulation time was set to the pulsar period P, allowing a spectrum to be obtained for each period. The correlator output, in the form of a set of auto- and cross-spectra, was recorded in an IDIFITS format file.

The dynamic spectrum is defined as a discrete sequence of spectra, $I^{\rm ab}(f_i,t_j)$,—a complex function of frequency, f, and time, t, where $i \in [0; N_{\rm ch}-1]$ is the spectral channel number, $j \in [0; N_{\rm p}-1]$ is the pulse number, $N_{\rm p}$ is the total number of pulses. Symbols "a" and "b" represent the interferometric baseline. We often use the magnitude of this quantity: $F^{\rm ab}(f_i,t_j) = \left|I^{\rm ab}(f_i,t_j)\right|$. To correct for the shape of the receiver's passband, variations in gain (automatic gain control was disabled in all experiments), and interference, the dynamic spectrum was normalized using the following relation

$$F^{\rm ab}_{\rm norm}(f_i,t_j) = \frac{F^{\rm ab}_{\rm ON}(f_i,t_j) - F^{\rm ab}_{\rm OFF}(f_i,t_j)}{F^{\rm ab}_{\rm OFF}(f_i,t_j)}. \qquad (1)$$

Here, $F^{\rm ab}_{\rm OFF}(f_i,t_j)$ is the average value of the dynamic spectra obtained in the windows outside the pulse. Any remaining significant interference was replaced by random values with the mean and variance determined from neighboring areas of the spectrum.

Typically, the dynamic spectrum displays regions with increased signal intensity, which we will refer to as scintles. Scintles are the visible manifestation of pulsar scintillation, arising due to the coherent summation of radio waves arriving from different parts of the scattering disk. The characteristic size of scintles in frequency is related to the size of the scattering disk, and their duration reflects the speed of the diffraction pattern's movement relative to the observer. To determine scintillation characteristics, we calculated a two-dimensional correlation function

$$DCCF(\Delta f_k,\Delta t_m) = \frac{\sum_{i=0}^{N_{\rm ch}-1}\sum_{j=0}^{N_{\rm p}-1} F_{ij}F_{i+k,j+m}}{(N_{\rm ch}-k)(N_{\rm p}-m)}, \qquad (2)$$

where $k \in [-N_{\rm ch}/2+1; N_{\rm ch}/2-1]$, $m \in [-N_{\rm p}/2+1; N_{\rm p}/2-1]$. Then, the decorrelation bandwidth, $\Delta f_{\rm dif}$, is defined as the half-width of the two-dimensional correlation function at zero time lag, $DCCF(\Delta f_k, 0)$, at half the maximum, and the scintillation time $\Delta t_{\rm dif}$ is the half-width at the level of $1/e$ of section, $DCCF(0,\Delta t_m)$. To more accurately determine these quantities, we approximated the sections using functions of the form

$$f(x) = A\exp(-(|x|/k)^m) + C. \qquad (3)$$

In this case, for a good approximation of $DCCF(\Delta f_k, 0)$ it is often necessary to introduce additional components symmetrically shifted relative to the main one. In such cases, the decorrelation bandwidth was taken as only the half-width of the central component.

The slope of the temporal structure function, α_t, is related to the power-law index of the spectrum of spatial inhomogeneities in the scattering plasma, n, as $n = \alpha_t + 2$ at $\Delta f \ll \Delta f_{\rm dif}$ [17]. The temporal structure function can be derived from the dynamic spectrum as

$$D_{\rm s}(\Delta t) = 2(DCCF(0,0) - DCCF(0,\Delta t_m)). \qquad (4)$$

However, the $DCCF(0,0)$ value is determined with significant error in practice, leading to unreliable determination of α_t. It is more convenient to work directly with the dynamic spectrum. For small Δf the approximating function can be represented as $f(x) \approx A[1-(|x|/k)^m] + B$, whence $D_{\rm s} = (|x|/k)^m$, i.e., $\alpha_t = m$. Here, all points of the $DCCF(0,\Delta t_m)$ function contribute equally to the approximation, allowing $DCCF(0,0)$ to be excluded from consideration. To determine α_t, we performed an approximation using function (3) for the section $DCCF(0,\Delta t_m)$ over the interval $|\Delta t_{\rm m}| < 0.5\Delta t_{\rm dif}$.

The amplitude of the visibility function on the baseline formed by telescopes "a" and "b" depends on the projection of the interferometer baseline as [18]:

$$B_{\rm ab}(b) = \exp\left[-\frac{1}{2}\left(\frac{\pi}{\sqrt{2\ln 2}}\frac{\theta_{\rm H} b}{\lambda}\right)^{n-2}\right], \qquad (5)$$

where b is the projected baseline, λ is the observing wavelength, and, $\theta_{\rm H}$ is the full width at half maximum (FWHM) of the scattering disk of the pulsar image. To determine $B_{\rm ab}$, we used the method outlined in [10]. It was shown that, in the case of strong scintillation, the

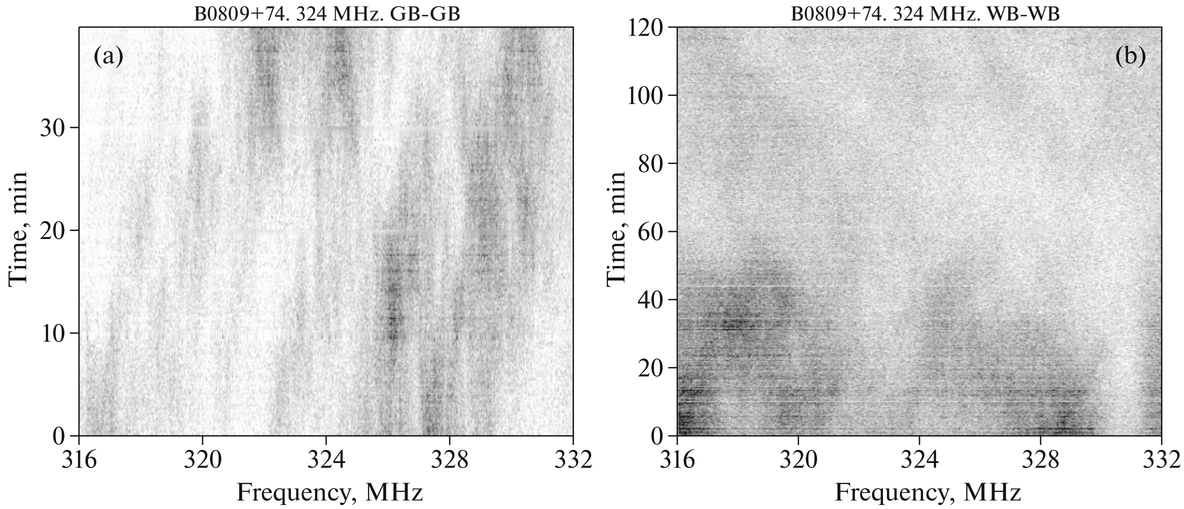

Fig. 1. Dynamic spectra of pulsar B0809+74 obtained during the experiments on (a) December 17, 2012 and (b) November 24, 2013. Darker regions correspond to greater intensity.

covariance function of the complex dynamic spectrum $J^{ab}(\Delta f) = \left|\langle I^{ab}(f,\mathbf{b})\bar{I}^{ab}*(f+\Delta f,\mathbf{b})\rangle\right|$ can be represented as the sum of two components: the frequency correlation function of flux fluctuations $B(\Delta f)$, which depends only on the frequency shift Δf, and the spatial coherence function $B(\mathbf{b})$, which depends only on the baseline projection:

$$J^{ab}(\mathbf{b},\Delta f) = \left|B(\Delta f)\right|^2 + \left|B(\mathbf{b})\right|^2. \quad (6)$$

Then, by comparing the values of J^{ab} at $\Delta f = 0$ and $\Delta f \gg \Delta f_{\rm dif}$, we can determine $B(\mathbf{b})$:

$$\left|B(\mathbf{b})\right| = \left(\frac{J^{ab}(\mathbf{b},\Delta f \gg \Delta f_{\rm dif})}{J^{ab}(\mathbf{b},0) - J^{ab}(\mathbf{b},\Delta f \gg \Delta f_{\rm dif})}\right)^{1/2}. \quad (7)$$

The scattering disk diameter is related to the spatial size of the diffraction spots in the observer's plane by the expression

$$\rho_{\rm dif} = \frac{\sqrt{2\ln 2}}{\pi\theta_{\rm H}}\lambda. \quad (8)$$

For a uniform distribution of scattering material along the line of sight, the scattering disk diameter is related to the scattering time, $\tau_{\rm sc} = (2\pi\Delta f_{\rm dif})^{-1}$, as $\theta_{\rm H,u} = (16\ln 2c\tau_{\rm sc}/D)^{1/2}$, where D is the distance to the pulsar, and c is the speed of light [19]. If all scattering material is concentrated in a thin layer at a distance, d, from the observer, this distance can be determined from the relationship between the measured scattering disk size, $\theta_{\rm H}$, and the theoretical value for a uniformly distributed scattering medium:

$$\frac{d}{D} = \left(1 + \frac{2\theta_{\rm H}^2}{\theta_{\rm H,u}^2}\right)^{-1}. \quad (9)$$

3. RESULTS

3.1. Pulsar B0809+74

Pulsar B0809+74 is relatively close, located at a distance of 433 pc, with a small dispersion measure [20]. This results in a wide decorrelation bandwidth and a long scintillation time at the observed frequency. Observations of this pulsar were conducted in two sessions: 40 min on December 17, 2012 and 2 h on November 24, 2013. In both cases, the ground-space baseline projection was near its maximum: 21.6 and 25.2 Earth diameters, respectively (see Table 1).

Only one ground telescope, Green Bank, participated in the session on December 17, 2012. The raw dynamic spectrum from this session was obtained with 4096 frequency channels. Such frequency resolution was excessive, so to improve the signal-to-noise ratio, we averaged it over four spectral channels and two pulsar periods. As a result, the frequency resolution was 15.625 kHz, and the time resolution was 2.58 s. The dynamic spectrum is shown in Fig. 1a.

Although the scattering material is thin for such a nearby pulsar, diffraction scintillation are still observed. In the dynamic spectrum, within the 16 MHz frequency band, distinct scintles are clearly visible, characteristic of strong scattering. From Fig. 1a, we can see that the scintle lifetime is around 20–30 min, only slightly shorter than the session duration, meaning some scintles were cut off. Upon closer inspection, most scintles have an internal structure: they appear to be composed of two smaller scintles.

The scintillation parameters for this pulsar, the decorrelation bandwidth, $\Delta f_{\rm dif}$, and scintillation time, $\Delta t_{\rm dif}$, were determined using equation (2) and approximating function (3) (see Fig. 2, two left panels). The frequency cross-section of the autocorrelation function is well described by a three-component function.

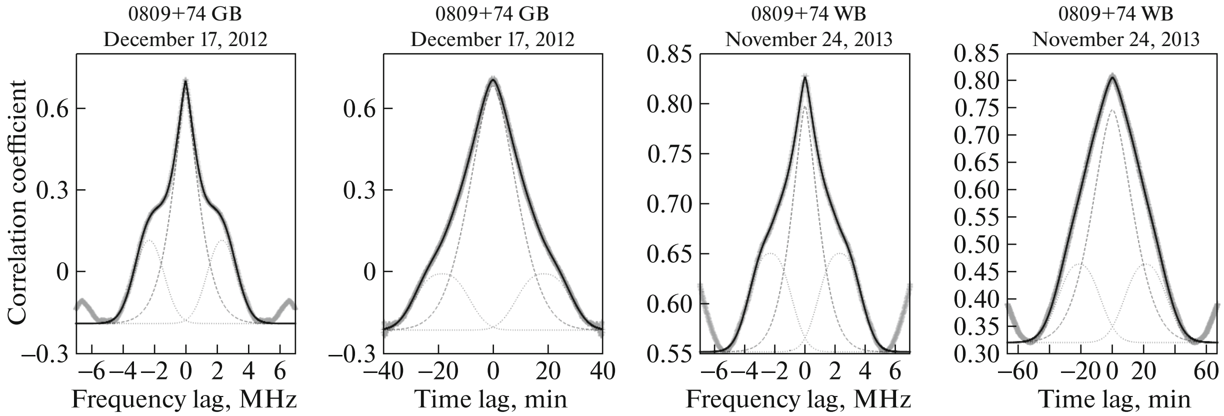

Fig. 2. Cross-sections of the two-dimensional autocorrelation functions of the dynamic spectra of pulsar B0809+74 by frequency and time, obtained in the experiments on December 17, 2012 (left) and November 24, 2013 (right). The gray thick solid line represents the observational data, while the black solid line represents the approximation result. Thin lines show the components of the approximating function. The decorrelation bandwidth and scintillation time were determined solely from the central (dashed line) component.

The presence of symmetrical side components, in addition to the central one, reflects the complex structure of the scintles. The decorrelation bandwidth, determined from the central component, was 940 ± 13 kHz, and the slope of the frequency structure function was 0.94 ± 0.04.

The time cross-section can also be formally approximated by a three-component function, yielding a scintillation time of 736 ± 3 s. However, due to the truncation of a significant portion of the scintles, caused by the short observation time, this value can only be considered a lower bound.

The spectral index of the spatial inhomogeneity spectrum, n, determined from the temporal structure function, was 3.51. It has been shown in [15] that when the observation time is less than several tens of $\Delta t_{\rm dif}$ the n value may be underestimated, which likely occurred in our case. Thus, the obtained value can also be considered a lower limit.

A year later, on November 24, 2013, the appearance of the dynamic spectrum changed dramatically. The original dynamic spectrum, obtained with the Westerbork telescope in 2048 frequency channels, was averaged over two spectral channels and three pulsar periods, resulting in a frequency resolution of 15.625 kHz and a time resolution of 3.87 s. The result is shown in Fig. 1b. In the lower part of the dynamic spectrum, several large scintles are visible during the first 50 min, showing a similarly complex structure as in the previous session. However, it is difficult to determine the characteristic size of these scintles. It is possible that we are observing several scintiles of similar size to those in the previous session, but many of them were truncated at the lower edge of the dynamic spectrum. Another possibility is that these are parts of two larger scintiles that filled almost the entire reception band, with portions observed at the beginning of the session. From the analysis of the autocorrelation function cross-sections of this dynamic spectrum (Fig. 2, two right panels), we obtained values $\Delta f_{\rm dif} = 1000 \pm 100$ kHz, $\Delta t_{\rm dif} = 1120 \pm 110$ s, and $n > 2.98$, which are in good agreement with the previous observation. However, if we indeed observed "large scintiles," these values would not even provide a rough estimate.

The remaining time, 1 h and 10 min, seems empty, but it is actually filled with a diffuse, low-contrast structure. The most likely explanation is that we are observing a transition from strong diffractive scintillation to weak refractive scintillation. The regime of Fresnel focusing, where the decorrelation bandwidth equals the observation frequency, separates these two modes.

The complex dynamic spectra on the ground baselines (Kalyazin–Westerbork) and ground-to-space baselines exceeding 20 Earth diameters did not show any scintillation structure. The covariance functions J^{ab} were indistinguishable for spectra obtained inside and outside the pulse window, making it impossible to estimate the spatial coherence function using equation (7).

3.2. Pulsar B0919+06

Observations of pulsar B0919+06 were conducted five times between 2015 and 2018 (see Table 1). The dynamic spectra for all five sessions are shown in Figs. 3a–3f.

They demonstrate significant variability between sessions, in the measured scintillation parameters. For example, the decorrelation bandwidth varied more than fivefold in 2018, but the value obtained three

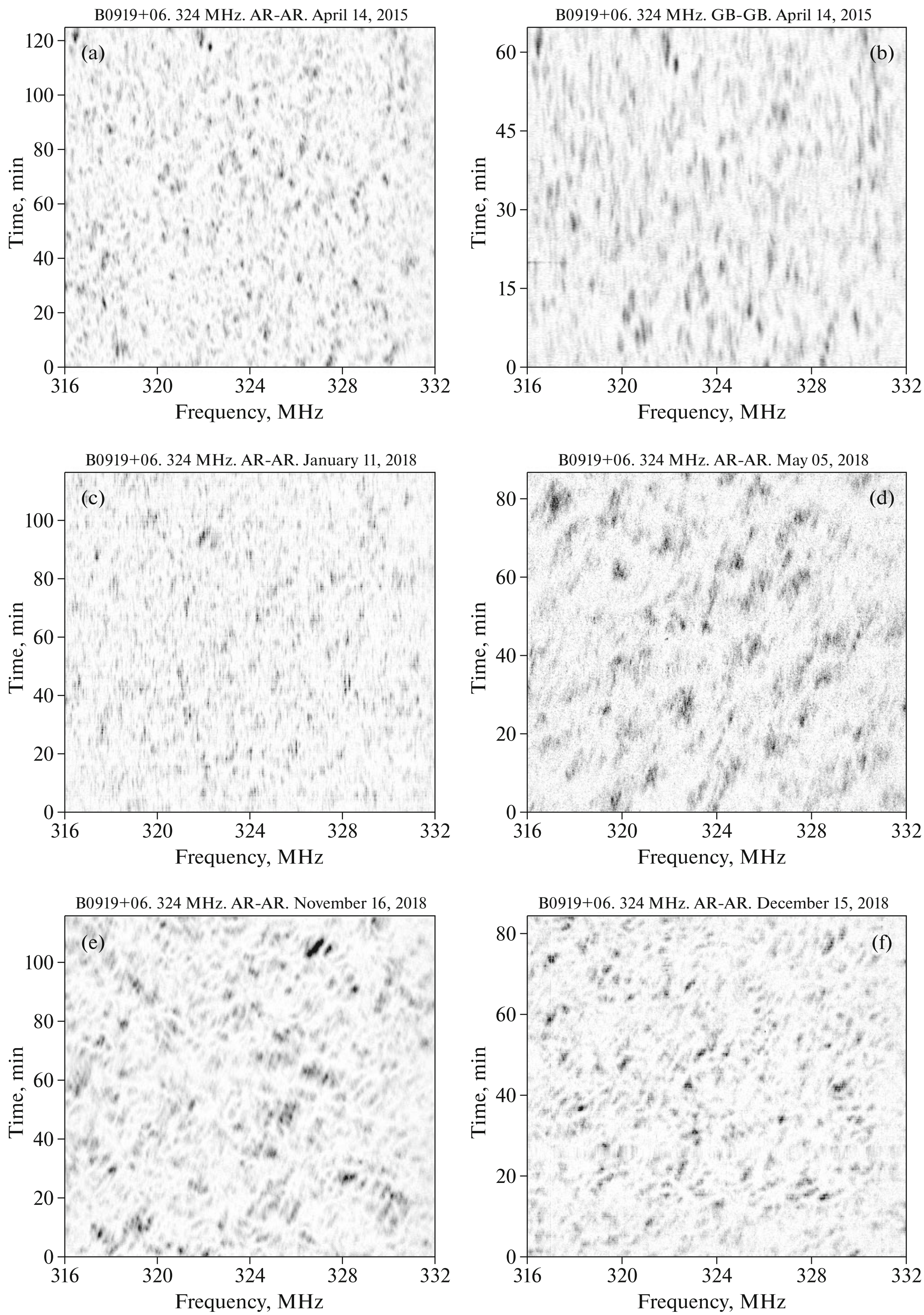

Fig. 3. Dynamic spectra of pulsar B0919+06.

Table 2. Scintillation parameters

Pulsar	Date	Δf_{dif}, kHz	Δt_{dif}, s	n	ρ_{dif}, $\times 10^3$ km	θ_{H}, mas	d/D		
							(a)	(b)	(c)
B0809+74	Dec. 17, 2012	940(13)	736(3)	>3.51					
B0809+74	Nov. 24, 2013	1000(100)	1120(11)	>2.98					
B091+06	Apr. 14, 2015	80.3(4)	118.5(17)	3.98(5)	>0.9	<80	0.66(5)	>0.015	>0.0006
B091+06	Jan. 11, 2018	36.2(6)	115(2)	3.95(6)	<70	>1		<0.55	<0.9
B091+06	May 10, 2018	195(13)	116(3)	3.80(5)	2.6(2)	28(2)		0.041(11)	0.0020(7)
B091+06	Nov. 16, 2018	131(8)	106.37(3)	4.18(16)					
B091+06	Dec. 15, 2018	133(1)	76(2)	3.895(3)	2.8(2)	26(2)		0.066(17)	0.0033(11)
B113+16	Feb. 4, 2014	348(2)	100(16)	3.4(2)					
B113+16	Feb. 3, 2018	100.2(3)	39.1(5)	3.48(13)	<86	>0.8		<0.8	<0.9
B113+16	Mar. 28, 2018	140.6(6)	47.1(3)	3.72(2)					
B113+16	Dec. 17, 2018	145(10)	117(6)	3.27(10)	6.0(8)	12.0(16)		0.072(13)	0.045(15)

The errors in units of the last given digits of the measured values are given in brackets. The value d/D (a) is obtained by calculating the delay time of the scintillation pattern between stations. The value d/D (b) is obtained from the time it takes the scintile to pass the observation point. The value d/D (c) is obtained using formula (9).

years earlier still falls within the range of variability seen in the later data. At the same time, the scintillation time exhibited far less variation. In the sessions on January 11 and May 10, 2018, which showed the most significant difference in decorrelation bandwidth, the scintillation times were consistent within the margin of error. The spectral index of plasma inhomogeneity, n, was close to 4 in all cases, suggesting a Gaussian, rather than Kolmogorov, distribution of inhomogeneities. The measured scintillation parameters are summarized in Table 2.

In the experiment on April 14, 2015, the scintillation pattern was clearly visible in the dynamic spectra obtained by both ground antennas. The observations at Green Bank started 60 min later than at Arecibo, so the overlap period of joint observations lasted only 1 h (see Fig. 4).

We divided the observation session into two 30-min segments and calculated the cross-correlation function of the dynamic spectra for each segment. In both segments, it was found that the scintillation pattern at Green Bank is ahead of that at Arecibo by just over 2 s on average. An example of the time cross-section of the correlation function is shown in Fig. 5a, and the inset in Fig. 5b shows the region around the maximum of the correlation function.

The time lag varies throughout the day due to the changing orientation of the baseline projection relative to the velocity vector of the scintillation pattern, V_{ISS}, in the observer's plane. Figure 5c shows the expected daily variation of the diffraction pattern lag with time of day. We estimated the velocity as $V_{\mathrm{ISS}} = 970 \pm 30$ km/s. During the fitting process, only V_{ISS}, was varied, while its direction was assumed to coincide with the pulsar's tangential velocity. The distance to the pulsar $D = 1210 \pm 190$ pc [21], and its proper motion $\mu_{\mathrm{p}} = 88.4 \pm 0.9$ mas/year [22]. From this, the pulsar's tangential velocity $V_{\mathrm{p}} = 510 \pm 90$ km/s, which exceeds both Earth's orbital velocity and likely the velocity of the scattering screen. Then, the relative distance to the screen

$$\frac{d}{D} = \frac{V_{\mathrm{ISS}}}{V_{\mathrm{p}} + V_{\mathrm{ISS}}} = 0.66 \pm 0.05, \tag{10}$$

which corresponds to the distance $d = 800 \pm 200$ pc from the observer.

We now turn to the determination of the scattering disk size. In the April 14, 2015 experiment, the visibility function amplitude, calculated using equation (7), was close to unity, i.e., the scattering disk was unresolved on the 2416 km Green Bank–Arecibo baseline. This implies the scattering disk size did not exceed 80 mas. Conversely, in the January 11, 2018 experiment, the scattering disk was fully resolved on the 131 000 km space–ground baseline, indicating its size was at least 1–2 mas. On May 10, 2018, the amplitude of the visibility function was measured on the intercontinental Arecibo–Westerbork baseline, yielding a scattering disk size of 28.2 mas. In the experiments on November 16 and December 15, 2018, the scattering disk was once again fully resolved.

The December 15, 2018 experiment was the most productive, as it allowed the measurement of $B(\mathbf{b})$ on several baselines. The left panel of Fig. 6 shows an example of the covariance function of the complex dynamic spectrum obtained on the Green Bank–Arecibo baseline in left circular polarization. Circles represent the covariance values for spectra outside the pulse window, and squares for those within the win-

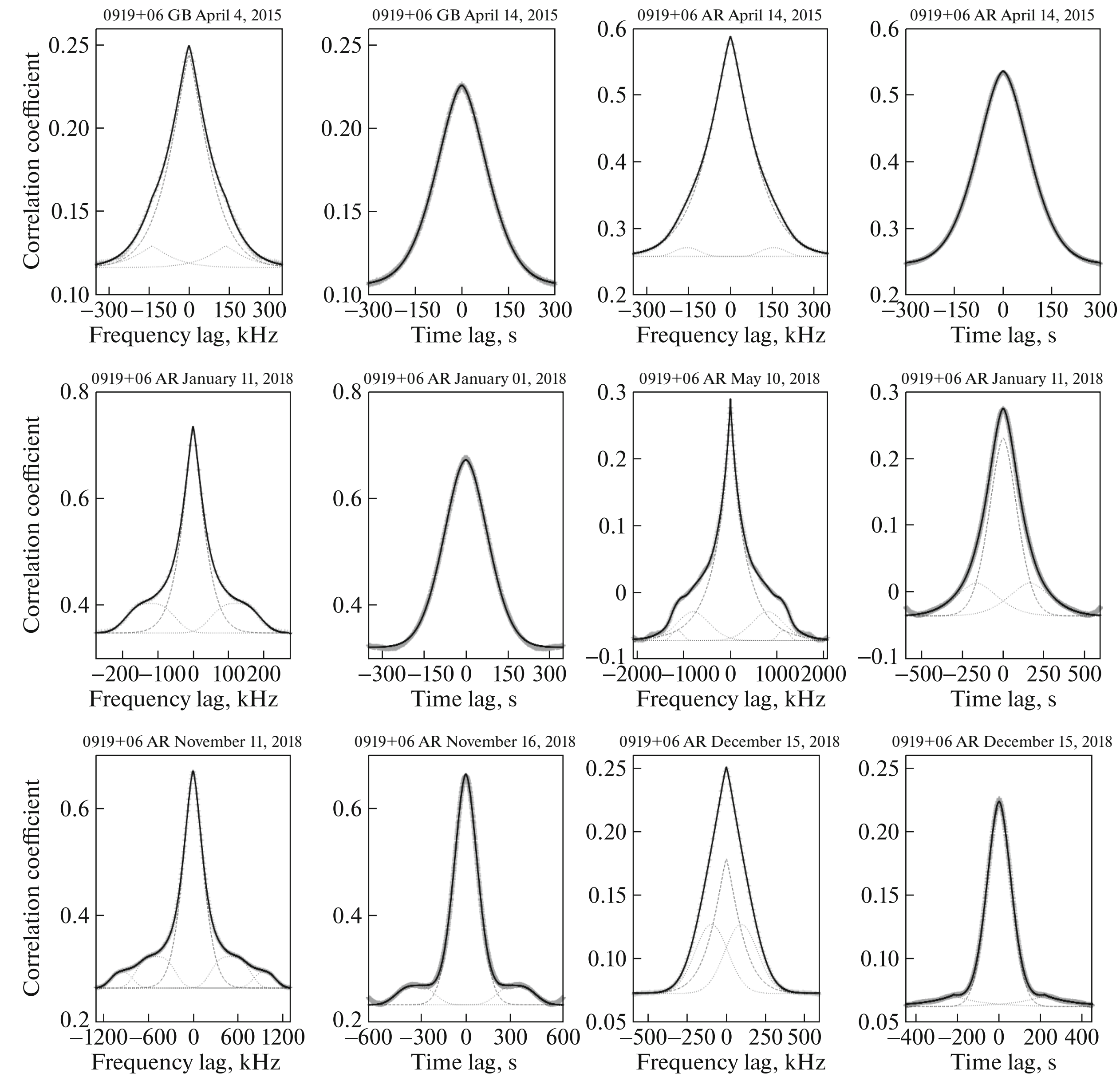

Fig. 4. Cross-sections of the two-dimensional autocorrelation functions of the dynamic spectra of pulsar B0919+06 at $\Delta t_m = 0$ (odd columns) and $\Delta f_n = 0$ (even columns). Thin dashed and dotted lines represent the components of the approximating function when there is more than one. The decorrelation bandwidth and scintillation time were determined only from the central (dashed line) component.

dow. For the plot, we averaged the covariance functions over 9 points, but for fitting, we used the data without averaging. The zero-shift value was not used for fitting either function. The solid line represents the fit for the covariance function within the pulse window, while the dashed line represents the fit outside the window. The J value outside the pulse window is constant, and it was treated as a zero level to determine $J^{ab}(0)$ and $J^{ab}(\Delta f \gg \Delta f_{dif})$. The right panel of Fig. 6 shows the dependence of the visibility function amplitude on the baseline projection. The $B(\mathbf{b})$ value was determined for the Arecibo–Westerbork and Green Bank–Arecibo baselines in both polarizations. The line shows the $B_u(b)$, dependence obtained from fitting the experimental values to the theoretical expression (5). The curve corresponds to a scattering disk diameter $\theta_H = 26 \pm 2$ mas. The formal error in the fitting is used as the uncertainty here. This value is close to the one obtained on May 10, 2018, six months earlier.

The position angles of the GB-AR and AR-WB baselines differ by almost 75°. Earlier, we implicitly

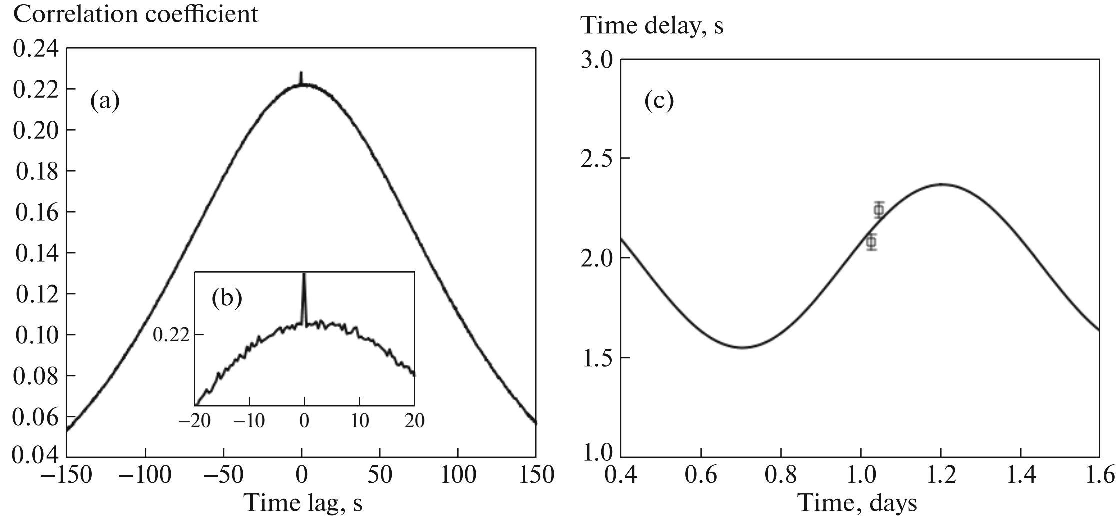

Fig. 5. Pulsar B0919+06, experiment on April 14, 2015. (a) Time slice of the mutual correlation function of the dynamic spectra from Arecibo and Green Bank. (b) An enlarged section of the covariance function near the maximum. The narrow peak at zero is related to the pulsar's power varying from pulse to pulse and does not depend on scintillations, while the broad part, shifted to the right, corresponds to scintile correlation. (c) Modeled delay dependence between the Green Bank and Arecibo antennas.

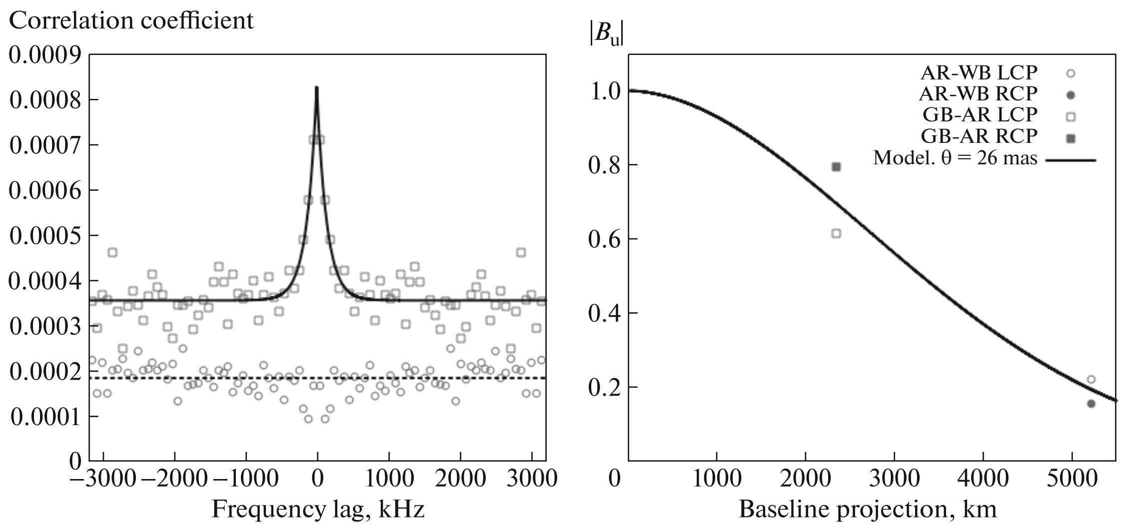

Fig. 6. Left: covariance functions of the dynamic spectrum of pulsar B0919+06 (December 15, 2018) on the Green Bank–Arecibo baseline during the pulse window (squares and solid line) and outside the pulse (circles and dashed line). Right: dependence of the amplitude of the visibility function on the projection length of the baseline. Circles show values obtained on the Arecibo–Westerbork baseline, while squares indicate the Green Bank–Arecibo baseline. Filled shapes represent right circular polarization, and unfilled shapes represent left circular polarization. The line represents the approximation of the values using formula (5).

assumed that the scattering disk of the pulsar is symmetric (a circle), although in some cases this is not true [6, 7, 23]. Nevertheless, the θ_H values calculated for each individual $B(\mathbf{b})$ vary within a small range of 20 to 30 mas, which suggests that the assumption of the scattering disk's symmetry is close to reality.

The spatial size of the diffraction spots in the observer's plane ρ_{dif}, calculated using formula (8), for both determined values of θ_H is 2600–2800 km. The diffraction spots pass through the antenna over time Δt_{dif}, from which we derive the speed of the diffraction pattern's movement $V_{ISS} = \rho_{dif}/\Delta t_{dif}$. It was 22 ± 2 km/s on May 10, 2018 and 36 ± 4 km/s on December 15, 2018, which is more than an order of magnitude smaller than the value obtained earlier for the session on April 14, 2015. From this, using formula (10), we calculate the distances to the scattering screens $d/D = 0.041 \pm 0.011$ and 0.066 ± 0.017 for the observations on May 10, 2018, and December 15, 2018, respectively.

This discrepancy in the estimates of V_{ISS} and consequently in the distances to the scattering screens between the 2015 and 2018 observations is too significant to ignore. The first point to note is that V_{ISS} in the two latest experiments are comparable to the orbital velocity of the Earth. If we do not neglect the movement of the screen V_S and the observer V_O, the velocity of the scintillation pattern can be expressed as a vector

$$\mathbf{V}_{ISS} = -\frac{d}{D-d}\mathbf{V}_P + \frac{D}{D-d}\mathbf{V}_S - \mathbf{V}_O. \quad (11)$$

Here, as before, we consider only the projections of the respective velocities onto the UV-plane. First, let us assume that $V_S = 0$ and consider the influence of the observer's velocity. In the experiments under consideration, V_O was 4.3 and 16 km/s, and the angles between its direction and the pulsar's velocity were 179.5° and 82.6°, respectively. Given that $V_P \gg V_O$, taking into account V_O hardly affects the distance estimate to the screen but can significantly alter the position angle V_{ISS}. On May 10, 2018, V_{ISS} was almost directly opposite to V_P, while on December 15, 2018, the deviation was 26°.

If we assume that the scintillation of the pulsar in the experiment on April 14, 2014 occurred on the same screen as during the later observations, then considering the observer's movement, the angle between the baseline projection and V_{ISS} would be approximately 68°, which is too small to reconcile the observed scintillation pattern delay between the antennas with V_{ISS}, which, according to our assumptions, should be around 27 km/s. Of course, it is possible that at different times, different regions of the interstellar medium located at different distances, dominate the scattering process [24], but a more likely reason for the discrepancy in the values seems to be neglecting the motion of the medium. Indeed, when the screen is located close to the observer, the coefficient before $\mathbf{V}_S$ in formula (11) is on the order of one, and screen velocities of several tens of kilometers per second are sufficient to noticeably change the direction of V_{ISS}.

The required distance to the scattering screen can be determined without using information about the scintillation pattern velocity. Formula (9) only requires knowledge of Δf_{dif} and θ_H, which were simultaneously measured in the same experiments on May 10, 2018, and December 15, 2018. Substituting the values, we obtain even closer screen positions: $d/D = 0.0020 \pm 0.0007$ and 0.0033 ± 0.0011, respectively.

3.3. Pulsar B1133+16

Pulsar B1133+16 exhibits sporadic pulse nulling, which accounts for about 15% of its signal spectrum. To exclude the influence of nulling on the correlation results, we slightly modified the procedure for processing the original dynamic spectra. It is known that the distribution of pulsar pulses by power is well described by a lognormal distribution. After constructing the distribution of pulses by power, we identified the weakest pulses, which were in excess compared to the lognormal distribution. Further, we averaged the dynamic spectra over three pulses, excluding nulls from the averaging. If the entire triplet of pulses consisted of nulls, the resulting value was obtained by averaging the values of adjacent triplets of pulses. As a result, the time resolution deteriorated to 3.65 s. The final dynamic spectra are shown in Fig. 7.

For the experiment on February 3, 2018, the use of 65 536 frequency channels proved excessive. Therefore, after processing with a median filter to remove impulsive noise, the data were averaged over 16 frequency channels. The resulting frequency resolution was 3.9 kHz.

Since the scintillation time turned out to be comparable to the interval between individual scans (30 s), we used only individual scans to determine it, and then averaged the results obtained from individual scans. Examples of cross-sections of the two-dimensional autocorrelation functions of the pulsar's dynamic spectra are shown in Fig. 8.

The distance to B1133+16 is approximately 372 ± 3 pc [24]. Despite the fact that this pulsar is located closer than B0809+74 and has a smaller dispersion measure, its scintillation parameters are closer to those of the more distant pulsar B0919+06. The obtained values, as with other pulsars, vary by a factor of 2–3 over time.

In the experiment on December 17, 2018, an interferometric signal was detected on both the ground-based and ground-to-space baselines. Figure 9 shows the dependence of the visibility function amplitude on the interferometer baseline projection. Fitting the values obtained only from ground-based baselines using formula (5) allows us to estimate the size of the scattering disk to be 12 mas. The formal error, 1.6 mas, is likely underestimated by several times, since, due to the limited reception band, the $J^{ab}(\Delta f \gg \Delta f_{dif})$ value does not tend to a constant with increasing Δf, but oscillates, which complicates the determination of B_u and introduces additional error into the measurements. On ground-to-space baselines, the visibility amplitude is significantly higher than expected according to expression (5). This phenomenon has been observed before and indicates that the interferometer resolves the substructure of the scattering disk on the largest baselines [5].

In this experiment, the dynamic spectra exhibited clearly visible features on two telescopes: Arecibo and Green Bank. Similarly to pulsar B0919+06, we attempted to measure the scintillation pattern delay between the stations. Averaging over three pulses greatly reduces the time resolution, and the abun-

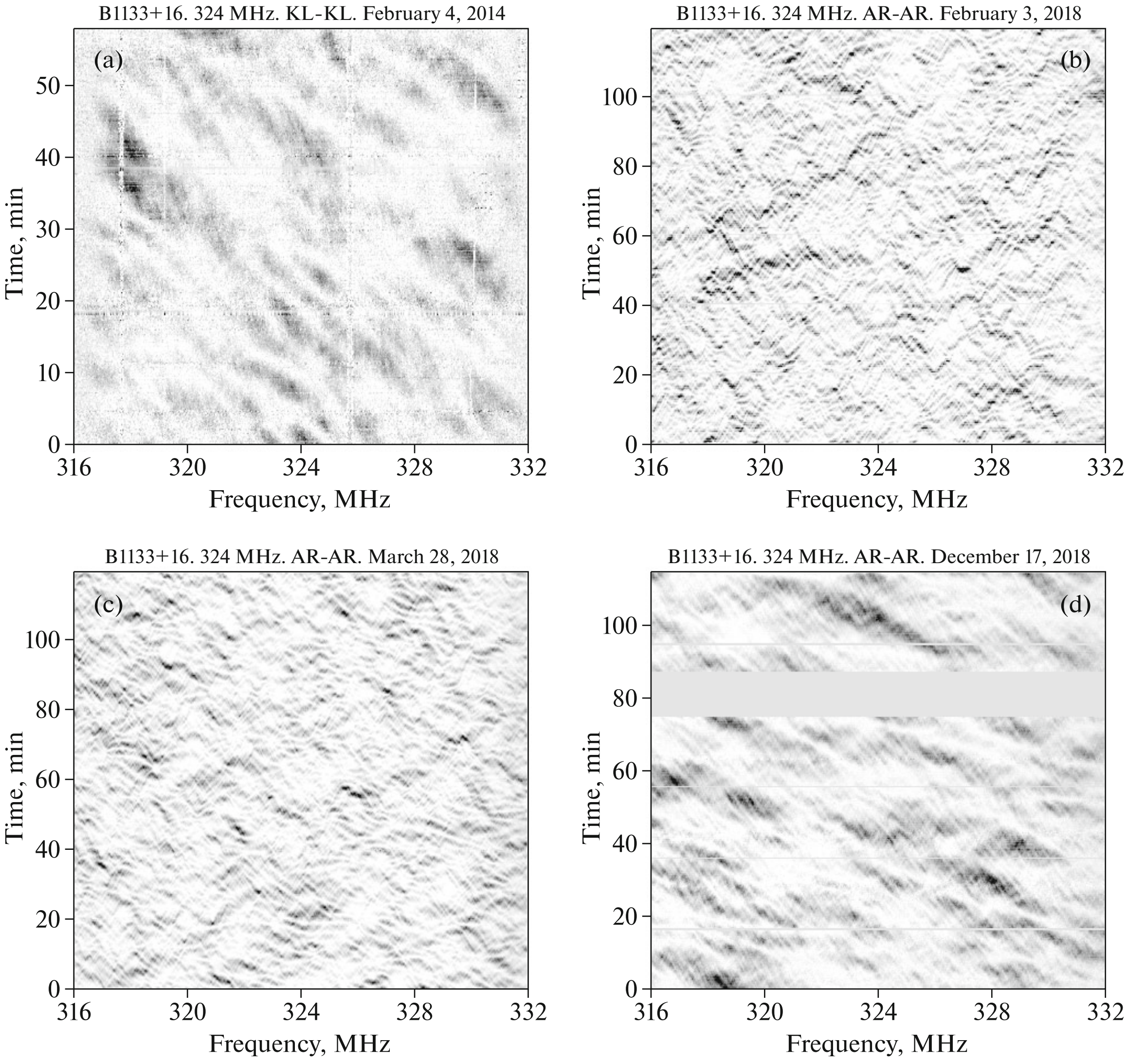

Fig. 7. Dynamic spectra of pulsar B1133+16.

dance of nulls leads to the cross-correlation of the spectra reflecting the correlation of nulls more than scintles. To improve measurement accuracy, we selected blocks of 20 pulses free from nulls in the dynamic spectra. Over two hours of observations, about 15 minutes of data were suitable for cross-correlation. We determined that the scintillation pattern was observed in Arecibo 0.5 ± 0.2 s later, which is half the pulsar's period, meaning we can only confidently say that the observed delay is small.

McKee et al. showed that five screens, labeled by the authors from B to F, are distinguished in the direction of this pulsar. These screens alternated in exhibiting scattering effects from 1980 to 2015 [24]. Screen F is located just 5.5 pc from the Sun, which is only 1.5% of the distance to the pulsar. According to formula (11), the contribution of the pulsar's tangential velocity $659.7^{+4.2}_{-4.5}$ km/s [24] to $V_{\rm ISS}$ becomes comparable to the observer's velocity of 7 km/s and the screen's velocity of 5.3 ± 0.4 km/s. Unfortunately, the direction of the screen's velocity is unknown, preventing any conclusion about the observed scintillation delay being related to this screen. The other screens are located at distances of 0.3 to 0.7 of the distance to the pulsar and may have velocities significantly exceeding the speed of sound in the interstellar medium, meaning they could greatly influence both the magnitude and direction of $V_{\rm ISS}$. It is also possible that scattering occurs simultaneously on multiple screens. Thus, the small measured scintillation pattern delay and the small (5°–21°) angle between the interferometer baseline projection and the pulsar's velocity direction during the observation indicate not a high $V_{\rm ISS}$ value, but rather a substantial difference between the pulsar's tangential velocity direction and the diffraction pattern's velocity relative to the observer.

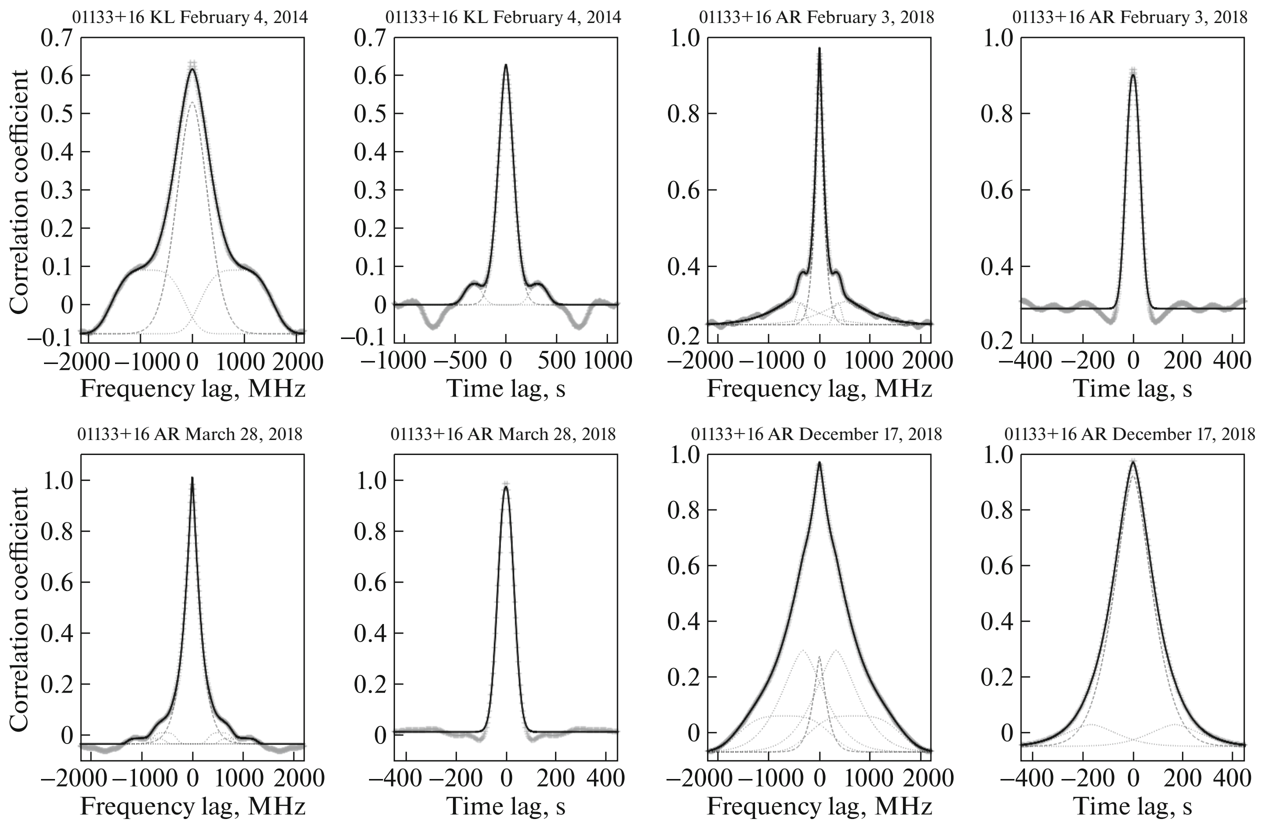

Fig. 8. Cross-sections of the two-dimensional autocorrelation functions of the dynamic spectra of pulsar B1133+16 at $\Delta t_m = 0$ (odd columns) and $\Delta f_n = 0$ (even columns). Thin lines represent components of the approximating function when more than one exists. The decorrelation bandwidth and scintillation time were determined only from the central (dashed line) component.

The measured scattering disk corresponds to a spatial size $\rho_{\rm dif} = (6.0 \pm 0.8) \times 10^3$ km, which, together with the measured scintillation time, gives an interference pattern speed of only 51.9 ± 9 km/s. This value contradicts scattering on screen F alone, as it cannot account for such a high $V_{\rm ISS}$ value. Nevertheless, such a velocity could lead to such a small scintillation pattern delay only if the pattern's motion is nearly perpendicular to the interferometer's baseline.

If the scattering medium were uniformly distributed, the size of the scattering disk would be only 3.6 mas. The size we measured is significantly larger, which requires the screen to be located near the observer. Using formula (9), we find that the screen is at a relative distance $d/D = 0.045 \pm 0.015$ or an absolute distance of 17 ± 5 pc. This is a very small distance where it is difficult to find notable gas structures that could scatter the radiation of a distant pulsar. On the other hand, the pulsar's galactic latitude is 69°, meaning it is located approximately 340 pc above the galactic plane, i.e., on the periphery of the stellar disk and significantly above the bulk of the interstellar gas. Therefore, the close proximity of the scattering screen appears quite plausible.

The experiment of February 3, 2018 involved only a ground-to-space baseline with the Arecibo telescope. The observation conditions were similar to those discussed above. We obtained a visibility function value of 0.08, even less than what was obtained on this baseline in the previously discussed experiment. Therefore, we can similarly conclude that the scattering disk is fully resolved on such a large baseline, and we can only set a limit: $\theta_{\rm H} > 0.8$ mas.

4. DISCUSSION

A detailed study of the scintillations of pulsar B0809+74 at frequencies below 111 MHz was previously conducted by Shishov and Smirnova [25]. Our n was systematically lower than their value of 3.7 ± 0.04, likely due to the small number of scintles that fully entered the dynamic spectrum, which is a result of the insufficient duration of the observation sessions. Adjustment of our $\Delta f_{\rm dif}$ and $\Delta t_{\rm dif}$ values to match those in their work using the relationships $\Delta f_{\rm dif} \propto f^{2n/(n-2)}$ and $\Delta t_{\rm dif} \propto t^{2/(n-2)}$ shows that the $\Delta f_{\rm dif}$ values in good agreement with the values obtained in [25], while the $\Delta t_{\rm dif}$ values are slightly underestimated, which is compatible with expectations.

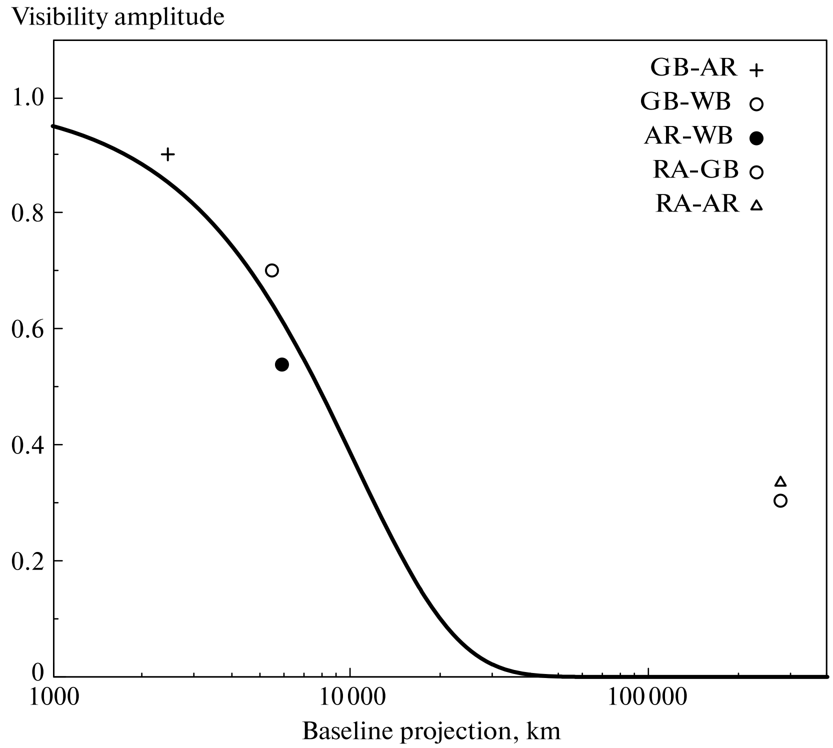

Fig. 9. Dependence of the amplitude of the visibility function on the projection length of the baseline for pulsar B1133+16 in the experiment on December 17, 2018. The approximation of the values for ground baselines is shown with a solid line.

For pulsar B0919+06, measurements of diffraction scintillation parameters Δf_{dif} and Δt_{dif} have been collected for nearly 20 years [26–28], primarily at frequencies of 327 and 430 MHz. Long-term observations have shown significant variability in these parameters [28]. For instance, at 327 MHz, they range from 120 to 400 kHz and from 60 to 230 s. Our measured values of diffraction parameters (Table 2) are close to the lower boundary of these ranges. Using these values, we can estimate the velocity of the diffraction pattern relative to the observer. For a Kolmogorov spectrum and a statistically homogeneous distribution of irregularities along the line of sight [29],

$$V_{\text{ISS,u}}\,[\text{km/s}] = A\frac{\sqrt{D\Delta f_{\text{dif}}}}{f\Delta t_{\text{dif}}}, \tag{12}$$

where $A = 2.53\times10^4$ km/s, Δf_{dif} is in MHz, D is in kpc, f in GHz, and Δt_{dif} is in s. Substituting our values into formula (12), we obtain the $V_{\text{ISS,u}}$ values for the five experiments—200, 140, 330, 290, and 410 km/s, respectively, which differs significantly from the values obtained in Subsection 3.2. If the interstellar plasma is non-uniform along the line of sight,

$$V_{\text{ISS}} = W_{\text{C}}\left[\frac{2d}{D-d}\right]^{1/2} V_{\text{ISS,u}}, \tag{13}$$

where W_{C} is a coefficient of approximately 1, which weakly depends on the spectrum of interstellar plasma irregularities [29]. Substituting the V_{ISS} and $V_{\text{ISS,u}}$ values obtained from the experiments on May 10, 2018, and December 15, 2018, we calculate relative distances of 0.002 and 0.004, respectively, which are in good agreement with our earlier conclusions. The value $V_{\text{ISS}} = 970$ km/s obtained previously from the diffraction pattern delay suggests that the direction of the pulsar's velocity coincides with the direction of the diffraction pattern's velocity, which is apparently not the case.

A joint analysis of astrometric observations of PSR B0919+06 and interstellar scintillation revealed that, in addition to the extended component of electron density in the direction of this pulsar, there is a scattering screen located less than 240 pc from the Sun [21]. Apparently, this screen influences the significant variability of the pulsar's diffractive parameters. Assuming the thickness of this screen to be 10 pc, the estimate of the dispersion measure is $10^{-3} < \Delta DM < 3\times10^{-2}$ pc/cm^3, which corresponds to an electron density of $10^{-4} < n_e < 0.003$ cm^{-3}. This is consistent with the DM variation of 4×10^{-3} pc/cm^3 for B0919+06 [30]. The average electron density at $DM = 27.271$ pc/cm^3 is 0.023 cm^{-3}.

This relatively close position of the screen generally is compatible with our measurements, although it significantly exceeds the distance to the screen that we determined. However, if a two-component model—consisting of a screen and an extended scattering component—is applied to analyze the obtained parameters, this would inevitably require moving the screen even closer to the observer [14], which seems implausible.

The discovery of parabolic structures (arcs) in the secondary spectra of pulsars [31] allowed the estimation of the distance to the screens and their properties. The theory of such arcs was developed in [32, 33]. Pulsar B0919+06 was one of the first pulsars for which the distance to the screen was estimated using this method: $d/D = 0.41$ and the corresponding size of the scattering disk was 3.6 mas [31]. Later, the same method demonstrated the existence of two screens at relative distances of 0.48 and 0.86 from the observer [34]. The theory of parabolic arcs requires that the scattered image of the pulsar be highly elongated, which is not confirmed by our measurements. When determining the distance, it is assumed that the direction of elongation of the scattering disk coincides with the direction of the effective velocity of the pulsar. If the angle between these directions is not zero, the position of the scattering screens should be closer to the observer. However, as this angle increases, the parabolic arcs in the secondary spectra disappear, making it impossible to fully reconcile our results with those obtained from the arcs.

The scintillation parameters $\Delta f_{\rm dif}$ and $\Delta t_{\rm dif}$ that we obtained for PSR B1133+16 show significant variability, changing by nearly a factor of 3.5 (see Table 2). In [28], observations conducted over 90 days at a frequency of 327 MHz exhibited similarly strong variability. This suggests that, in addition to the extended component, there are highly scattering screens along the line of sight. This is further supported by our measurements: the size of the scattering disk is nearly four times greater than that corresponding to scattering by uniformly distributed scattering plasma.

The presence of scattering screens in the direction of PSR B1133+16 has been reported in several studies [35–38]. It has been shown that there are six scattering screens in the direction of this pulsar, appearing in secondary spectra in various combinations at different times [24]. For five of these screens, distances, motion velocities, and angles of their velocities with respect to the major axis of the pulsar's scattering disk have been measured. The nearest detected screen is located at a distance of 5.46 pc from the Sun, which is close to our measured value; however, it has a negligible proper motion and therefore cannot account for the observed difference in the directions of $V_{\rm P}$ and $V_{\rm ISS}$. Other screens have a high velocity but are located significantly farther than the distance we determined. On the other hand, our analysis does not allow us to differentiate multiple screens from each other if they are acting simultaneously, and their cumulative effects can take various forms.

Modeling the brightness distribution in the scattering disk of the pulsar based on the analysis of secondary spectra indicated that the pulsar's image is highly elongated, with characteristic sizes of 13×2 mas [39]. The maximum size is close to the result of our measurements, but it should be noted that we assumed a symmetric image of the pulsar in our analysis.

5. CONCLUSIONS

Using the ground-to-space interferometer RadioAstron, we conducted a study of the scintillations of three radio pulsars: B0809+74, B0919+06, and B1133+16. By comparing the measured scattering parameters—such as the decorrelation bandwidth, scintillation time, size of the scattering disk, and the spectral index of spatial inhomogeneities in the scattering plasma—we estimated the distance to the scattering screens, which turned out to be relatively small. By comparing the dynamic spectra obtained from different antennas, we found that knowing only the velocity and direction of the pulsar's motion is insufficient to describe the movement of the diffraction pattern in the observer's plane. It appears that the scattering medium has its own quite high velocity, leading to a significant discrepancy between the direction of motion of the diffraction pattern and the direction of the pulsar's tangential velocity.

ACKNOWLEDGMENTS

This publication uses the results of pulsar observations conducted as part of the RadioAstron project at the following radio telescopes: the 100-m radio telescope of the Green Bank Observatory, the 300-m radio telescope of the Arecibo Observatory, the 64-m radio telescope of the Kalyazin Radio Astronomy Observatory, the Westerbork interferometer (only one 25-m telescope after 2013), and the 64-m telescope of the National Institute for Astrophysics in Italy, located in Sardinia.

FUNDING

The RadioAstron project was led by the AstroSpace Center of the Lebedev Physical Institute of the Russian Academy of Sciences and the Lavochkin Research and Production Association under a contract with the State Space Corporation ROSCOSMOS, in collaboration with many scientific and technical organizations in Russia and other countries.

CONFLICT OF INTEREST

The authors of this work declare that they have no conflicts of interest.

REFERENCES

1. N. W. Broten, J. L. Locke, T. H. Legg, C. W. McLeish, and R. S. Richards, Nature (London, U.K.) **215** (5096), 38 (1967).
2. N. S. Kardashev, A. V. Alakoz, A. S. Andrianov, M. I. Artyukhov, et al., Vestn. NPO Lavochkina, No. 3 (33), 4 (2016), https://elibrary.ru/download/elibrary_26421217_17562386.pdf.
3. N. S. Kardashev, A. V. Alakoz, A. S. Andrianov, U. Baan, et al., Vestn. NPO Lavochkina, No. 3 (41), 3 (2018). https://elibrary.ru/download/elibrary_36328394_55227639.pdf.
4. C. R. Gwinn, M. V. Popov, N. Bartel, A. S. Andrianov, et al., Astrophys. J. **822**, 96 (2016); arXiv: 1501.04449 [astro-ph.GA].
5. M. V. Popov, N. Bartel, C. R. Gwinn, M. D. Johnson, et al., Mon. Not. R. Astron. Soc. **465**, 978 (2017); arXiv: 1609.04008 [astro-ph.HE].
6. M. V. Popov, A. S. Andrianov, M. S. Burgin, V. A. Zuga, A. G. Rudnitskii, T. V. Smirnova, V. A. Soglasnov, and E. N. Fadeev, Astron. Rep. **63**, 391 (2019).
7. T. V. Smirnova, V. I. Shishov, A. S. Andrianov, M. S. Burgin, et al., Mon. Not. R. Astron. Soc. **496**, 5149 (2020).
8. N. Bartel, M. S. Burgin, E. N. Fadeev, M. V. Popov, N. Ronaghikhameneh, T. V. Smirnova, and V. A. Soglasnov, Astrophys. J. **941**, 112 (2022); arXiv: 2210.16669 [astro-ph.GA].
9. T. V. Smirnova, V. I. Shishov, M. V. Popov, C. R. Gwinn, et al., Astrophys. J. **786**, 115 (2014); arXiv: 1402.6346 [astro-ph.GA].
10. V. I. Shishov, T. V. Smirnova, C. R. Gwinn, A. S. Andrianov, M. V. Popov, A. G. Rudnitskiy, and V. A. Soglasnov, Mon. Not. R. Astron. Soc. **468**, 3709 (2017); arXiv: 1605.05727 [astro-ph.SR].
11. A. S. Andrianov, T. V. Smirnova, V. I. Shishov, C. Gwinn, and M. V. Popov, Astron. Rep. **61**, 513 (2017).
12. M. V. Popov, A. S. Andrianov, N. Bartel, C. Gwinn, B. C. Joshi, D. Jauncey, N. S. Kardashev, A. G. Rudnitskii, T. V. Smirnova, V. A. Soglasnov, E. N. Fadeev, and V. I. Shishov, Astron. Rep. **60**, 792 (2016).
13. E. N. Fadeev, A. S. Andrianov, M. S. Burgin, M. V. Popov, A. G. Rudnitskiy, V. I. Shishov, T. V. Smirnova, and V. A. Zuga, Mon. Not. R. Astron. Soc. **480**, 4199 (2018); arXiv: 1801.06099 [astro-ph.GA].
14. E. N. Fadeev, Res. Astron. Astrophys. **18** (8), 103 (2018); arXiv: 1805.07983 [astro-ph.GA].
15. M. V. Popov and T. V. Smirnova, Astron. Rep. **65**, 1129 (2021).
16. M. V. Popov, Astron. Rep. **66**, 1311 (2022).
17. V. I. Shishov, T. V. Smirnova, W. Sieber, V. M. Malofeev, et al., Astron. Astrophys. **404**, 557 (2003).
18. C. R. Gwinn, J. M. Cordes, N. Bartel, A. Wolszczan, and R. L. Mutel, Astrophys. J. **334**, L13 (1988).
19. M. C. Britton, C. R. Gwinn, and M. J. Ojeda, Astrophys. J. **501**, L101 (1998); arXiv: astro-ph/9610028.
20. W. F. Brisken, J. M. Benson, W. M. Goss, and S. E. Thorsett, Astrophys. J. **571**, 906 (2002); arXiv: astro-ph/0204105.
21. S. Chatterjee, J. M. Cordes, T. J. W. Lazio, W. M. Goss, E. B. Fomalont, and J. M. Benson, Astrophys. J. **550**, 287 (2001); arXiv: astro-ph/0010060.
22. R. S. McGary, W. F. Brisken, A. S. Fruchter, W. M. Goss, and S. E. Thorsett, Astron. J. **121**, 1192 (2001); arXiv: astro-ph/0010374.
23. W. F. Brisken, J. P. Macquart, J. J. Gao, B. J. Rickett, W. A. Coles, A. T. Deller, S. J. Tingay, and C. J. West, Astrophys. J. **708**, 232 (2010); arXiv: 0910.5654 [astro-ph.GA].
24. J. W. McKee, H. Zhu, D. R. Stinebring, and J. M. Cordes, Astrophys. J. **927**, 99 (2022); arXiv: 2112.11980 [astro-ph.HE].
25. T. V. Smirnova and V. I. Shishov, Astron. Rep. **52**, 736 (2008).
26. J. M. Cordes, J. M. Weisberg, and V. Boriakoff, Astrophys. J. **288**, 221 (1985).
27. J. M. Cordes and A. Wolszczan, Astrophys. J. **307**, L27 (1986).
28. N. D. R. Bhat, A. P. Rao, and Y. Gupta, Astrophys. J. Suppl. **121**, 483 (1999); arXiv: astro-ph/9810354.
29. J. M. Cordes and B. J. Rickett, Astrophys. J. **507**, 846 (1998).
30. J. A. Phillips and A. Wolszczan, Astrophys. J. **385**, 273 (1992).
31. D. R. Stinebring, M. A. McLaughlin, J. M. Cordes, K. M. Becker, J. E. E. Goodman, M. A. Kramer, J. L. Sheckard, and C. T. Smith, Astrophys. J. **549**, L97 (2001); arXiv: astro-ph/0010363.
32. M. A. Walker, D. B. Melrose, D. R. Stinebring, and C. M. Zhang, Mon. Not. R. Astron. Soc. **354**, 43 (2004); arXiv: astro-ph/0403587.
33. J. M. Cordes, B. J. Rickett, D. R. Stinebring, and W. A. Coles, Astrophys. J. **637**, 346 (2006); arXiv: astro-ph/0407072.
34. M. L. Putney and D. R. Stinebring, Chin. J. Astron. Astrophys. Suppl. **6** (S2), 233 (2006).
35. A. S. Hill, D. R. Stinebring, C. T. Asplund, D. E. Berwick, W. B. Everett, and N. R. Hinkel, Astrophys. J. **619**, L171 (2005); arXiv: astro-ph/0411752.
36. D. R. Stinebring, Chin. J. Astron. Astrophys. Suppl. **6** (S2), 204 (2006).
37. D. Stinebring, Astron. Astrophys. Trans. **26,** 517 (2007).
38. D. R. Stinebring, B. J. Rickett, and S. K. Ocker, Astrophys. J. **870**, 82 (2019); arXiv: 1811.04519 [astro-ph.GA].
39. F. S. Trang and B. J. Rickett, Astrophys. J. **661**, 1064 (2007); arXiv: astro-ph/0702210.

Translated by M. Chubarova

Publisher's Note. Pleiades Publishing remains neutral with regard to jurisdictional claims in published maps and institutional affiliations.
AI tools may have been used in the translation or editing of this article.